Edinburgh Research Explorer

Methane scattering on porous kerogen surfaces and its impact on mesopore transport in shale

Link:
Link to publication record in Edinburgh Research Explorer

Document Version:
Peer reviewed version

Published In:
Fuel

OPEN ACCESS

Methane scattering on porous kerogen surfaces and its impact on mesopore transport in shale

Yichong Chen[a,*], Jun Li[b,*], Saikat Datta[a], Stephanie Docherty[c], Livio Gibelli[a,*], Matthew K. Borg[a]

[a]*School of Engineering, University of Edinburgh, Edinburgh EH9 3FB, United Kingdom*
[b]*Center for Integrative Petroleum Research, College of Petroleum Engineering and Geosciences, King Fahd University of Petroleum and Minerals, Dhahran 31261, Saudi Arabia*
[c]*School of Computing, Engineering and Physical Sciences, University of the West of Scotland, Paisley PA1 2BE, United Kingdom*

Abstract

Revealing the scattering behaviour of gas molecules on porous surfaces is essential to develop accurate boundary conditions for kinetic transport models that describe the gas dynamics in shale reservoirs. Here, we use high-fidelity molecular dynamics simulations to resolve the gas-surface interactions between methane molecules and realistic organic kerogen surfaces, and to assess the applicability of the widely used scattering kernels. Our results show that the tight matrix porosities have a negligible effect on the timescale and lengthscale of the scattering process, which can be considered instantaneous in time and local in space. Although reflected velocity distributions reveal that the common Maxwell, Cercignani-Lampis and Yamamoto scattering models fail to fully capture the scattering details of methane on kerogen, especially when the incident molecular speeds are high, the Maxwell model predicts best the reflected angular beam pattern and the overall reflected velocity distribution for rough kerogen surfaces. However, for low-speed impingement, more characteristic of shale applications, all scattering models give similar velocity distributions, which are driven by the high degree of gas-surface accommodation observed. We find that a Maxwell model with a calibrated tangential momentum accommodation coefficient, which approaches unity as the surface roughness increases to ~ 2 nm, is enough to reproduce comparable velocity profiles and mass flow rates inside moderately confined kerogen mesopores. Deviations between the Maxwell model and our molecular simulations are only observed for highly rarefied transport problems, but this rarefaction lies beyond the realm of shale reservoir applications. This paper, therefore, reports the first scattering study on porous and rough kerogen surfaces, and demonstrates the applicability of the Maxwell model, which can be readily incorporated into gas kinetic solvers to predict the apparent permeability of shale with mesopore and macropore networks.

Keywords: scattering kernels, organic kerogen, surface roughness, accommodation coefficient, molecular dynamics, rarefied gas dynamics

---

[*]Corresponding authors.
Email addresses: `yichong.chen@ed.ac.uk` (Yichong Chen), `junli@kfupm.edu.sa` (Jun Li), `livio.gibelli@ed.ac.uk` (Livio Gibelli)

1. Introduction

The recent shale gas revolution is transforming the global energy sector. Understanding the fundamental engineering science underpinning the extraction of methane gas from shale reservoirs is, therefore, becoming increasingly important [1]. Much of the unknown flow physics occurs at the micro/nano scales surrounding the organic kerogen structures [2–6], with micropores (< 2 nm) and mesopores (< 50 nm) being responsible for the major storage of methane in shale reservoirs. Moreover, adsorption [7, 8] and diffusive/advective transport [9] must be accounted for within these pores, where the interplay between these processes remains unclear [10, 11].

At a fundamental level, the physics at the micro/nano scales of shale applications is non-intuitive and depends on many physico-chemical phenomena. First, due to the large surface-area-to-volume ratio, the gas molecules interact as frequent with the pore surface as the interactions among themselves, which means effects like surface adsorption and surface diffusion can be significant. Secondly, because reservoirs operate at various pressures, from high (e.g. 50-100 MPa) all the way down to hundreds of kPa [12], there is a mix of dense and rarefaction effects in the different pores at different points in time of a reservoir's lifetime. The degree of rarefaction is generally described by the Knudsen number $Kn = \lambda/H$, where λ is the mean free path of the gas molecules, and H is the characteristic length of the flow system (such as the local pore width). Fluid flows in shale mesopores are in the slip ($0.001 < Kn < 0.1$) and transition ($0.1 < Kn < 10$) regimes [13], where the continuum assumption of classical flows is not valid, and transport properties can no longer be predicted accurately by the Navier-Stokes equations with no-slip boundary conditions [14, 15]. The Boltzmann equation and its model equations are applicable for mesopores, where confinement effects are negligible (e.g., $H > 7$ nm) [16, 17]. A number of kinetic solvers have been developed to solve the Boltzmann equation or a model of the kinetic equation, and to deal with various types of low-speed flows required in shale reservoirs, including in 3D geometries, such as the Direct Velocity Method (DVM) [18, 19], or the direct simulation BGK (DSBGK) method [20]. However, the overarching open question that has arisen in this field is whether an appropriate kinetic boundary condition exists for shale applications, which may contain molecular adsorption/desorption processes inside the tight porous surface.

These types of kinetic boundary conditions have been formulated for other engineering systems, such as for flows through micro-electro mechanical systems (MEMS) [14] or aerodynamics applications around very low earth orbits [21]. The way in which gas molecules scatter at a surface has led to several gas-surface interaction (GSI) models (known also as scattering kernels), such as the Maxwell model [22] and Cercignani-Lampis (CL) model [23]. Despite the recent emergence of these kinetic solvers in the field of shale gas modelling [24], high fidelity scattering studies of shale rock surfaces are, however, still missing.

The two questions that we aim to answer in this paper are: (a) can existing scattering kernels be used for shale, or new ones need to be developed? and (b) How do adsorption/desorption timescales, roughness and porosity of the organic kerogen affect the scattering dynamics of methane molecules? To answer both questions, we use high-fidelity molecular dynamics (MD) simulations, and realistic kerogen samples to provide insights of the scattering physics

2

and a baseline assessment of existing scattering kernels. We then analyse independently how the different scattering kernels lead to distinct predictions of gas transport, through mesopores confined by kerogen surfaces.

The remainder of this paper is organised as follows. The background on scattering kernels is described in Section 2. Section 3 introduces the methodology used in this work, including the MD set-up that resolves the scattering trajectories of methane gas molecules on kerogen surfaces. In Section 4, the MD results are used to answer the two questions above. Finally, the conclusions of this work and future outlooks are given in Section 5.

2. Background to scattering kernels

A scattering kernel permits one to relate the incident and reflected molecular fluxes for each possible incident velocity on a surface of interest, in the form of a probability density function (PDF). Without loss of generality, the probability density of all molecular scattering instances is given by $R(v' \rightarrow v; x' \rightarrow x; t' \rightarrow t' + \tau)$. This defines the probability a gas molecule strikes the surface at point x' and time t' with a velocity range $[v', v' + dv']$, and which then reflects away from the surface at a point x with a velocity range $[v, v + dv]$ after an elapsed time interval τ. In rarefied gas solvers, where this probability density is required as a form of boundary condition, scattering details are simplified by assuming a gas molecule re-emerges at the same point of a solid wall, after a negligible interaction time τ with the wall. The kinetic boundary condition is therefore normally described via a simplified scattering kernel, $R(v' \rightarrow v)$, which satisfies the basic properties of (a) positiveness, (b) normalisation, and (c) detailed balance [25] (see further details in Appendix A). Note that all the scattering kernels reported in this paper fulfil these properties. Furthermore, the Maxwell and CL models are investigated in this work since they are both classical models and are able to represent a large class of scattering kernels. The Yamamoto model [26] is considered in this work as well, since it is a combination of these classical models.

2.1. Maxwell model

The most famous and extensively used kernel was proposed by Maxwell [22]. The Maxwell model assumes that a fraction of the incident gas molecules is fully accommodated to the wall at a temperature T_w (i.e., molecules can be scattered to any direction with a uniform probability distribution, independent of their incident velocities v'), whereas the remaining molecules are re-emitted specularly. In the case of fully accommodated molecules, their reflection follow the fully diffuse scattering kernel, $R_d(v' \rightarrow v)$, which is given by:

$$R_d(v' \rightarrow v) = \frac{m^2 v_n}{2\pi (k_B T_w)^2} \exp\left(-\frac{mv^2}{2k_B T_w}\right). \tag{1}$$

Therefore, the diffuse-specular Maxwell scattering kernel is written as

$$R_M(v' \rightarrow v) = \sigma_t R_d(v' \rightarrow v) + (1 - \sigma_t)\delta(v' - v + 2nv_n), \tag{2}$$

where the constant σ_t is the tangential momentum accommodation coefficient (TMAC), defined within a range $[0, 1]$, n represents the unit vector perpendicular to the surface and pointing into the gas region, and δ is the Dirac delta function.

3

2.2. Cercignani-Lampis (CL) model

Unlike phenomenological models [27–31], the CL model [23] has been physically derived, and can reproduce the lobular pattern shown by molecular beam experiments. In the CL model, the change of the momentum and energy are quantified by two accommodation coefficients, one for the tangential momentum σ_t, and one for the normal component of the kinetic energy α_n. The CL model is written as

$$R_{CL}(\boldsymbol{v}' \rightarrow \boldsymbol{v}) = \frac{1}{2\pi} \frac{1}{\alpha_n \sigma_t (2 - \sigma_t)} \frac{v_n}{(\frac{k_B}{m} T_w)^2} I_0 \left(\frac{\sqrt{1 - \alpha_n} |v_n'| v_n}{\alpha_n \frac{k_B}{m} T_w} \right)$$
$$\times \exp \left\{ -\frac{v_n^2 + (1 - \alpha_n)|v_n'|^2}{2\frac{k_B}{m} T_w \alpha_n} - \frac{[\boldsymbol{v}_t - (1 - \sigma_t)\boldsymbol{v}_t']^2}{2\frac{k_B}{m} T_w \sigma_t (2 - \sigma_t)} \right\}, \qquad (3)$$

where $\boldsymbol{v}_t$ is the two dimensional vector representing the tangential velocity. Note that the CL model simplifies to fully-diffuse scattering if $\sigma_t = \alpha_n = 1$, specular scattering for $\sigma_t = \alpha_n = 0$, and backward scattering (fully inverted velocity) for $\sigma_t = 2, \alpha_n = 0$.

2.3. Yamamoto model

Extensions have been made to the CL model [26, 32–35]. For example, Yamamoto *et al.,* [26] suggested using a bimodal distribution by assuming a fraction of molecules follow the quasi-CL model, while the remaining molecules are diffusely reflected. Similar to the CL model, the scattering process tangential to the surface is isotropic and is independent of the process normal to the surface in the Yamamoto model, which can be written as

$$R_{Y,t_1} = (1 - \sqrt{1 - \sigma_t^P}) \left(\frac{2\pi k_B T_w}{m} \right)^{-\frac{1}{2}} \exp \left(-\frac{m v_{t_1}^2}{2 k_B T_w} \right) + \sqrt{1 - \sigma_t^P} \left(\frac{2\pi \sigma_t^P k_B T_w}{m} \right)^{-\frac{1}{2}} \exp \left\{ -\frac{(v_{t_1} - \sqrt{1 - \sigma_t^P} v_{t_1}')^2}{2\frac{k_B}{m} T_w \sigma_t^P} \right\},$$
$$(4)$$

$$R_{Y,n} = (\alpha_n^P)^2 \frac{v_n}{\frac{k_B}{m} T_w} \exp \left(-\frac{m v_n^2}{2 k_B T_w} \right) + [1 - (\alpha_n^P)^2] \frac{v_n}{\frac{k_B}{m} T_w \alpha_n^P} I_0 \left(\frac{\sqrt{1 - \alpha_n^P} |v_n'| v_n}{\frac{k_B}{m} T_w \alpha_n^P} \right) \exp \left\{ -\frac{v_n^2 + (1 - \alpha_n^P)|v_n'|^2}{2\frac{k_B}{m} T_w \alpha_n^P} \right\}, \quad (5)$$

where v_{t_1} is the one-dimensional velocity tangential to the surface (i.e., v_x, v_y), σ_t^P is the partial TMAC and α_n^P is related to the partial kinetic energy accommodation normal to the surface (see Section 4.2 for more details). Although the bimodal distribution of the Yamamoto model is still determined by two accommodation coefficients, it provides more accurate fits compared to the CL model, based on observed scattering characteristics at a contaminated surface [26].

2.4. Scattering kernels in shale

As the scattering physics for kerogen/mineral surfaces remains poorly understood, there is a tendency to use simple scattering kernels, such as specular-diffuse or backward-diffuse (i.e., the combination of backward and diffuse scattering) in shale applications [19, 36, 37]. However, the weighting factor of diffuse scattering TMAC in these kernels is often treated as a convenient tuneable parameter to fit the effective permeability of experiments, with used

4

values ranging from 0.01 to 1.0 [37–40] (i.e., ranging from purely frictionless surfaces to complete diffuse), which raises confusion in the implementation of scattering kernels. For instance, Wu *et al.,* [40] claim TMAC should be as low as 0.5 and 0.1 to explain the experimental observation in the permeability-pressure curve. Beside the dispute about what TMAC value to choose, scattering on realistic shale surfaces should include the effects of porosity, roughness, adsorption, low-speeds flows and elevated pressures/temperatures, making it much different from the scattering on the controllable metal surfaces, on which most of scattering kernels are developed [26, 34, 35, 41, 42].

3. Modelling and Methodology

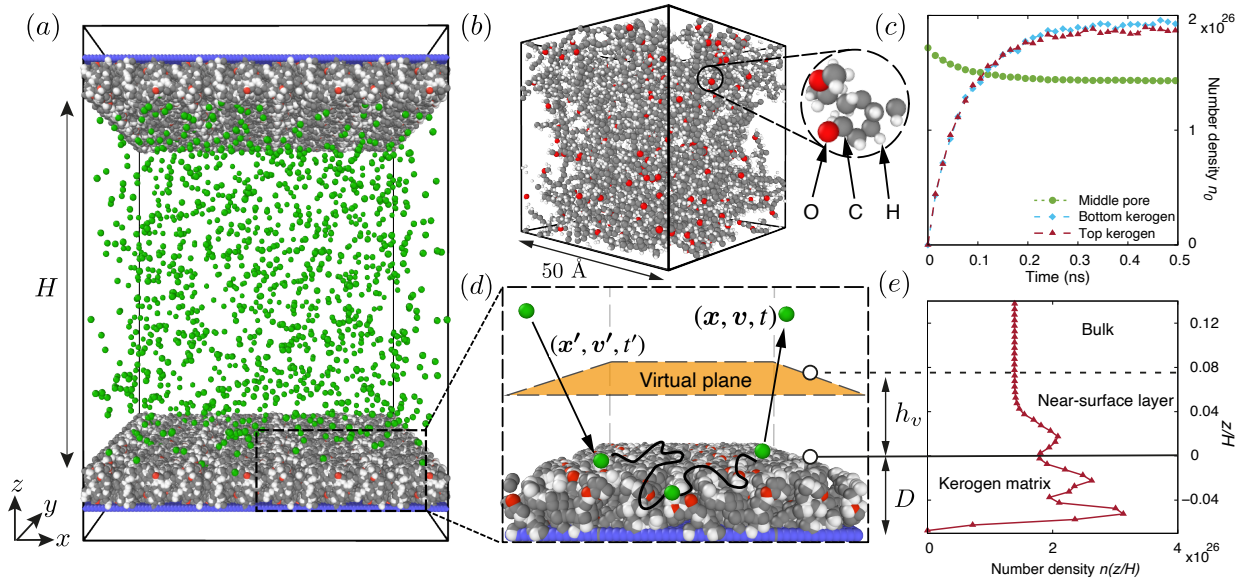### 3.1. Molecular Dynamics (MD) simulations

Figure 1: (a) Schematic of the MD domain, comprising methane flow through a quasi-2D pore slit constructed from two parallel kerogen walls with a width H = 20 nm; Colour legend: grey = carbon (C); white = hydrogen (H); red = oxygen (O); blue = outer-edge barrier (B); green = single-site methane (CH_4). (b) Kerogen structure EFK 0.8 g/cm^3 obtained from Bousige *et al.* [43]; (c) Number density of methane molecules in the bulk of the pore slit and inside the two kerogen walls during the equilibration run. (d) Schematic of the scattering process. Scattering information for incoming $(\boldsymbol{x'}, \boldsymbol{v'}, t')$ and outgoing $(\boldsymbol{x}, \boldsymbol{v}, t)$ molecules are recorded at the virtual plane (orange). (e) Number density profile of methane molecules across the pore slit after equilibration, corresponding to a bulk pore pressure P_0 = 0.81 MPa. Apart from the adsorption inside the kerogen matrix, monolayer adsorption is observed within the near-surface layer, which is defined by the distance h_v between the virtual plane (dashed line) and the kerogen surface (solid line).

In this work, we use the LAMMPS software [44] for running MD simulations of molecular scattering on realistic kerogen surfaces. MD resolves deterministically the trajectories of gas molecules and their van der Waals interactions with the wall atoms, by numerically integrating Newton's equations of motion, thereby enabling the molecular scattering to be accurately recorded. Fig. 1(a) shows the 3D MD set-up used in this work, which consists of methane stored inside a pore slit confined between two parallel kerogen walls. The distance between walls in the $z-$direction

5

Table 1: Interatomic Lennard Jones potential parameters (σ, ϵ) used in our MD simulations. Potential parameters for pairs of species not shown in the table are taken to be zero.

Atom pairs	σ [Å]	ϵ [kcal/mol]
CH_4-CH_4	3.730	0.2941
CH_4-B	3.545	0.0050
CH_4-C	3.545	0.1279
CH_4-H	3.075	0.0936
CH_4-O	3.450	0.2135

is taken to be the pore width H, while periodic boundary conditions are applied in the x, y directions. The kerogen samples used in this work are obtained from Bousige *et al.* [43], which were constructed using hybrid reverse Monte Carlo and MD simulations to match experimental properties, such as the pore size distribution, C-C pair distribution function and elastic properties. In this work we only show results for the Eagle Ford field kerogen (EFK), which is a low-maturity organic sample taken from a carbonate-rich shale reservoir. However, as discussed in Section 4, we do not expect any major differences in the scattering results if other kerogen samples are considered. The molecular structure for EFK has been calibrated for four different densities (i.e., porosities ϕ): 0.8 g/cm^3 (45%), 1.0 g/cm^3 (35%), 1.2 g/cm^3 (24%) and 1.4 g/cm^3 (14%) [43]. Each kerogen sample has a unit box size of 50 Å, as shown in Fig. 1(b). To achieve more statistics in our measurements, and apply more controlled edits to the surface roughness (see Section 4.2), the EFK sample was replicated in the x, y directions using multiples of its length, 50 Å. However, the thickness of the kerogen slab D, is taken to be smaller than 50 Å to save computational cost, since the scattering pattern is found to be independent of D when it is set larger than the interaction cut-off distance between gas molecules and surface atoms. To set the temperature of the kerogen samples, while keeping their structure similar to their equilibrium calibrated condition, a spring force is applied independently to each kerogen atom. The spring force tethers each atom to its initial position, at which the motion of each atom is solved using Langevin dynamics, with a damping parameter of 50 fs. Besides the kerogen structure, each parallel wall has a rigid single-layer barrier (B), which prevents any loss of methane molecules from the computational domain. Methane (CH_4) molecules are modelled using a monatomic model [43], which has been calibrated in previous work to describe the properties of methane as well as its adsorption in kerogen, as shown by experiments [43].

In our simulations, the velocity-Verlet algorithm with a time step of 0.5 fs was used to integrate the molecular trajectories, and all atoms (except the atoms in the kerogen matrix) interact using a standard 12-6 Lennard-Jones (LJ) potential

$$U_{LJ}(r) = 4\epsilon \left[\left(\frac{\sigma}{r} \right)^{12} - \left(\frac{\sigma}{r} \right)^6 \right],\qquad(6)$$

where r is the distance between the pair of atoms, σ is the distance at which the interatomic potential is zero (approximately equal to the diameter of an atom), and ϵ is the depth of the potential well. The interaction parameters

for all species considered in our MD simulations, which again are obtained from Bousige *et al.* [43] and Obliger *et al.* [45], are listed in Table 1. The interactions between the kerogen atoms (i.e., C-C, H-H and O-O) are substituted by a tethered harmonic spring force with a fixed spring constant 100 kcal/(mol Å^2) and a Langevin dynamics model. The value for $\epsilon_{\mathrm{CH_4-B}}$ is taken to be very small ~ 0.005 kcal/mol, which is an order of magnitude smaller than the kerogen-methane interactions. The small value of B-CH$_4$ interaction is necessary to avoid molecules from leaving the computational domain, and acts like a specular wall. To balance accuracy with computational efficiency, the long range interaction of the LJ potentials are cut-off at a distance $r = r_c = 15$ Å, using the neighbour list algorithm. This is within standard cut-off lengths of $r_c = 3 \sim 4\sigma$, around which the degree of accommodation for the GSI was shown to be invariant [46].

Each MD simulation run consists of two steps, namely an equilibration run and a production run. Initially, methane is placed only in the kerogen slit, and then the system is equilibrated for 0.5 ns at a constant temperature of 423 K, which is a value that can be reached in shale reservoirs [1, 45]. As shown in Fig. 1(c), this is enough time to allow methane molecules to adsorb inside the kerogen sample and reach a steady state in our cases, although the time for methane to adsorb is also proportional to the kerogen thickness and pressure within the slit pore [47]. During equilibration, the temperature of methane is kept constant using a Nosé-Hoover thermostat with a time constant of 100 fs in the NVT ensemble. Following equilibration, the MD simulation is run for a further 2-4 ns to produce the scattering data (see Section 3.2). During the production run, temperature control on the methane molecules is switched off, so not to bias their scattering dynamics.

3.2. Tracking gas-wall collisions

The definition of GSI from these deterministic simulations relies on tracking the gas molecules' positions and velocities at every time step, and selecting molecules that undergo a collision with the wall. For a hard-sphere fluid this is straightforward, since a collision with the wall happens instantaneously, thereby making it easy to obtain v' and v, while $x' \approx x$ and $\tau \approx 0$. However, for the continuous LJ potential considered in this work, which is required to accurately model the adsorption force field of the organic matrix, the definition of a wall collision is ambiguous. Here, as shown in Fig. 1(d), we define a *virtual plane* placed parallel to the surface of the wall at a distance h_v, beyond which the long-range attractive force of the kerogen's atoms are no longer felt by methane molecules, i.e., $h_v = r_c$. The *near-surface layer* within h_v will also contain adsorption and molecule ordering, as indicated in Fig. 1(e). When a gas molecule crosses the virtual plane from bulk and into the near-surface layer, the molecule's position, velocity and time are recorded (x', v', t'), which is the incident particle information. The molecule will also be recorded again when it crosses the virtual plane back into the bulk (x, v, t), which represents the reflected particle information. As illustrated in Fig. 1(d), the crossings of molecules across the virtual plane will contain modelling details about the GSI, and consequently, the incident and reflected information for every molecule colliding with the wall can be readily used to provide further physical insights, such as in the residence time and velocity distribution functions.
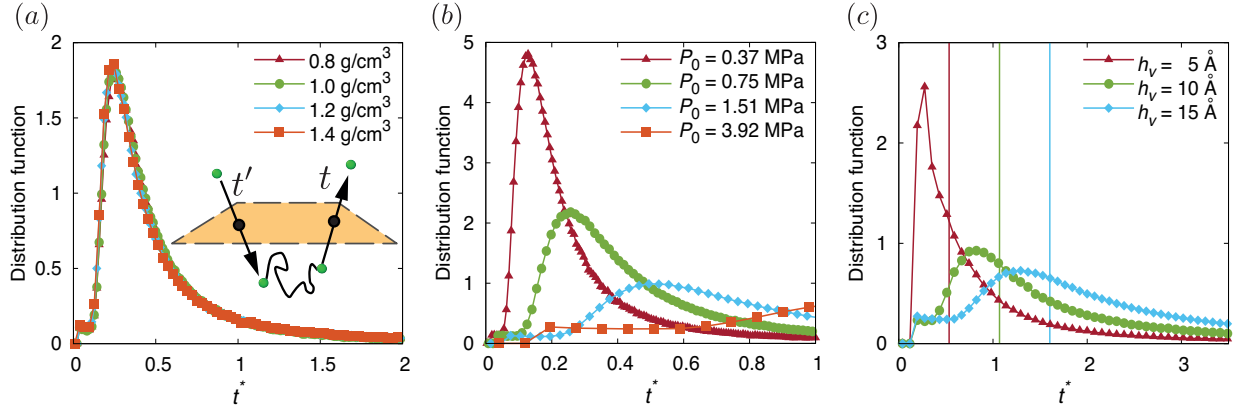
Figure 2: Distribution function of the nondimensional residence time ($t^* = \tau/\tau_c$) during the scattering of methane molecules inside the near-surface layer. The comparisons are performed for (a) various EFK kerogen porosities at a fixed bulk gas pressure ($P_0 = 0.95$ MPa) within the pore slit, (b) molecular systems of various pressures on kerogen structure EFK 0.8 g/cm^3, corresponding to $Kn = 1.28, 0.64, 0.31, 0.12$, respectively, and (c) various near-surface layer thicknesses at $P_0 = 3.92$ MPa on EFK 0.8 g/cm^3. Vertical lines represent the estimated time for molecules to cross the near-surface layer twice ($2h_v$) without considering adsorption, at a velocity $\sqrt{2\pi k_B T_0/m}/2$.

4. Results and Discussions

4.1. Effect of porous surfaces on gas scattering theory

As discussed in Section 2, the most widely used scattering kernels rely on the assumption that molecules striking the surface are instantaneously re-emitted from the impact position; i.e., $x' = x$ and $\tau = 0$. These assumptions, however, are questionable when considering porous surfaces, such as in organic matter considered here, in which a larger number of gas molecules can adsorb and desorb in the interstices of the microscale-thick matrix [6, 48], and diffusion playing a dominant role in the sorption processes. To assess the influence of a porous surface, especially on whether the assumption of negligible residence time and position locality of the GSI breaks down, we conducted a series of validation tests on these organic kerogen surfaces.

First, kerogen surfaces with various densities (or porosities) are investigated. We measured the residence time τ of gas molecules within the near-surface layer (and the porous kerogen matrix), which is given as the time interval $\tau = t - t'$. In Fig. 2(a), we show the results as a time distribution normalised by the characteristic time, i.e., the inverse of the gas-gas collision frequency $\tau_c = \sqrt{m/(\pi k_B T_0)}/4n_0\sigma_0^2$, where k_B is the Boltzmann constant, and T_0, σ_0 are the temperature and diameter of the methane molecules, respectively. Although the peaks of the normalised residence time distributions are not strictly close to zero, most of the gas molecules are re-emitted from the kerogen surface in a timescale $t^* = \tau/\tau_c$ smaller than unity, indicating the assumption of instantaneous scattering turns out to be reasonable. Note that this conclusion also depends on how the characteristic time τ_c has been defined, which is relative to the value of the gas number density n_0. It is seen that the time distribution curves almost coincide with each other, which indicates that the kerogen's matrix porosity has a negligible influence on the timescale of the re-emitted gas molecules. In this respect, one can further envision that any desorbed molecules, which were adsorbed inside the
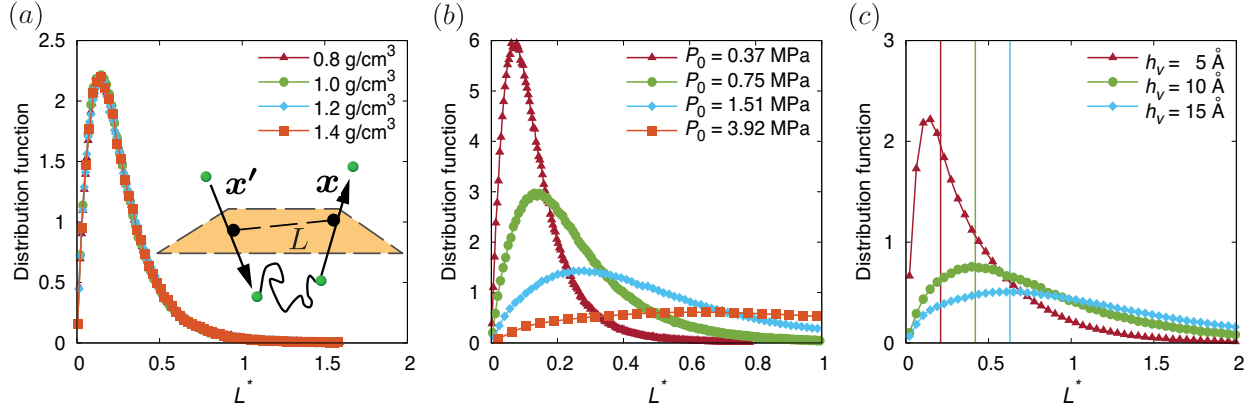
8

Figure 3: Distribution function of the nondimensional displacement ($L^* = L/\lambda$) during the scattering of methane molecules inside the near-surface layer. The comparisons are performed for (a) various EFK kerogen porosities at a fixed bulk gas pressure ($P_0 = 0.95$ MPa) within the pore slit, (b) molecular systems of various pressures on kerogen structure EFK 0.8 g/cm^3, corresponding to $Kn = 1.28, 0.64, 0.31, 0.12$, respectively, and (c) various near-surface layer thicknesses at $P_0 = 3.92$ MPa on EFK 0.8 g/cm^3. Vertical lines represent the thickness of the near-surface layer h_v.

kerogen for a long time, only contribute to a very small percentage of wall scattering events.

Next, we consider systems with different bulk pore pressures P_0, which are obtained by varying the number of methane molecules in the system. Note that in the considered range of pressure [0.37 - 3.92] MPa, the fluid is only slightly non-ideal, as the reduced number density is much smaller than unity. This remark can also be supported by evaluating the value of the compressibility factor [6] that turns out to be about 0.9882. This clearly proves that one can safely apply the ideal equation of state and, therefore, the Knudsen number of the molecular system can be evaluated as $Kn = \sqrt{2}/(2\pi H n_0 \sigma_0^2)$ for simplicity. Here, the corresponding Kn are considered lies in the transition regime. As the characteristic time τ_c used for the normalisation decreases with increasing P_0, a peak with $t^* > 1$ will be observed for high pressures (e.g., $P_0 = 3.92$ MPa in Fig. 2(b)), which means the timescale of most molecules resident within the near-surface layer is larger than the timescale of gas-gas interactions. In Section 4.4, we found that the impact of $t^*_{\text{peak}} > 1$ for these high pressure cases is negligible on the gas transport in a moderately confined pore slit with a size of 20 nm, and we expect this impact to be even smaller for larger pore sizes.

To explore further the contributing factors of t^*, we focus on the high pressure gas case and place the virtual plane at 5 Å, 10 Å and 15 Å away from the surface, respectively. This is purely a theoretical exercise, to demonstrate the sensitivity of the virtual plane location on t^*, and mechanisms leading to larger t^*. Fig. 2(c) shows that the residence time for the highest probability of scattering t^*_{peak} is lowered when the thickness of the near-surface layer h_v is reduced, which indicates that molecules spend less time travelling to the wall and back. Additionally, the average travelling time of molecules from the virtual plane to the wall and back is estimated using the normal component of the average velocity of diffusely reflected molecules $\sqrt{2\pi k_B T_0/m}/2$, with results shown as vertical lines in Fig. 2(c). Although porosities and attractive forces between gas molecules and surface increase the average residence time of molecules [49], the vertical lines closely match the t^*_{peak} of the respective curves, which tells us that most molecules are spending
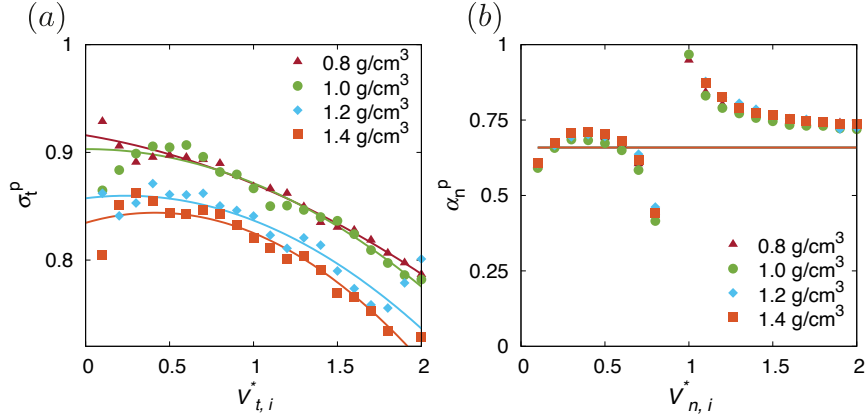
9

Figure 4: Partial accommodation coefficients calculated by MD simulations on kerogen structure EFK with different densities/porosities. Variation of (a) partial TMACs σ_t^P, and (b) partial α_n^P due to different incident velocities on the clean cut kerogen surfaces.

their time travelling in the near-surface layer in a quasi-collisionless state. The long tail of t^* highlights the few molecules that remain in an adsorbed state (or where gas-gas molecular interactions exist) with increased residence time. These tests prove that molecular adsorption has a small influence on the peak timescale of scattering t_{peak}^*. As shown in Figs. 3(a-c), a similar test has been performed in terms of the transverse scattering lengthscale. The displacement $L = \|x - x'\|$ of one molecule undergoing a scatter event has been evaluated and normalised by the mean free path λ of the gas molecules, i.e., $L^* = L/\lambda$. The magnitude of the displacement still largely depends on the thickness of the near-surface layer h_v, as indicated in Fig. 3(c), and similar arguments can be made about L_{peak}^*. Since both L^* and t^* are sensitive to the choice of h_v, this dependence raises the question about the appropriate location of the boundary in transport simulations using a scattering model, i.e., whether it should be defined at $z_0 = 0$ (as is more practical and also reduces t^*, L^* values below 1) or $z_0 = h_v$ (as is theoretically more accurate), which we discuss later on.

4.2. Origins in the gas-surface accommodation

Although conventional scattering kernels can still be used for shale applications, the degree of accommodation for momentum and energy of gas molecules with the surface needs to be investigated in the form of accommodation coefficients, to understand the scattering dynamics and suggest a suitable model. In this study, global accommodation coefficients are calculated using all the incident molecules irrespective of their velocity magnitude, while partial accommodation coefficients are evaluated by taking molecules with an incident velocity between $V_i^* - \Delta V^*$ and $V_i^* + \Delta V^*$, where the subscript i indicates incident molecules and the small increment $\Delta V^* = 0.1$. Since the particle dynamics is assumed to be decoupled in the tangential and normal directions, V_i^* can be referred as the tangential velocity component $V_{t,i}^*$ or the normal velocity component $V_{n,i}^*$ depending on the coefficient to be evaluated. Note that the asterisk denotes dimensionless quantities, and velocities are normalised by the most probable speed $V_m = \sqrt{2k_B T_w/m}$.
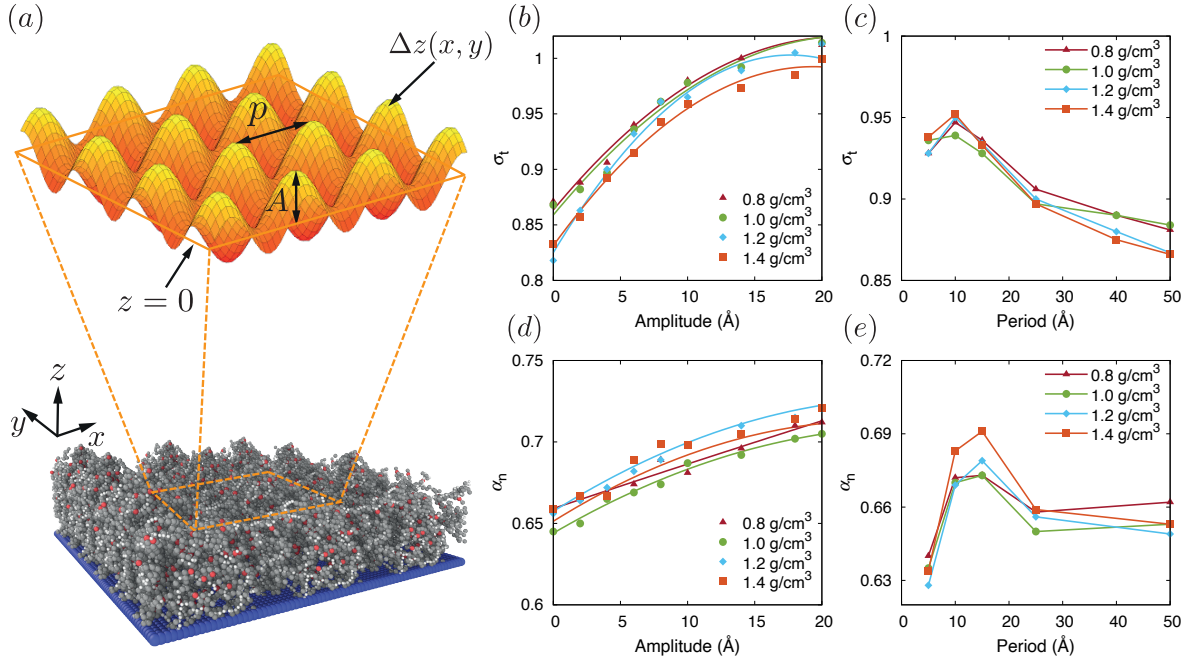
10

Figure 5: The effects of mesoscopic roughness on the degree of accommodation. (a) Schematic of the mesoscopic roughness on EFK kerogen structure, achieved by a 2D corrugated surface (orange). Variation of global TMACs due to different (b) roughness amplitudes A with period p = 25 Å, and (c) roughness periods p with A = 4 Å. Variation of global α_n due to different (d) roughness amplitudes A with p = 25 Å, and (e) roughness periods p with A = 4 Å.

Both global and partial accommodation coefficients follow the general form of the equation [25, 46, 50]

$$\alpha_\kappa = \frac{\langle \kappa_i \rangle - \langle \kappa_r \rangle}{\langle \kappa_i \rangle - \langle \kappa_s \rangle}, \tag{7}$$

where κ represents a generic scattering property, i.e., the velocity tangential to the surface or the normal component of the kinetic energy. The angle brackets denote the mean value, and the subscript r denotes the reflected molecules. The subscript s indicates that molecules are fully accommodated to the surface. α_κ thus can be readily derived based on the measurement from our MD simulations, and replaced by σ_t or α_n in Eqn. (7).

Extensive experimental [51, 52] and simulation work [41, 50, 53] have been conducted to find the relation between the accommodation coefficients and their influencing factors, such as gas temperature, gas molecular mass, surface topography, as well as the strength of the gas-surface intermolecular force field. To investigate the role of roughness on these porous surfaces, we distinguish between (a) *microscopic roughness*, which is inherent due to the micro porous nature of the kerogen, and (b) *mesoscopic roughness*, which stems from the mesoscopic topography of the surface. Realistic kerogen surfaces have both microscopic roughness (which is mostly dictated by local porosity) and mesoscopic roughness at the interface between the kerogen matrix and the larger mesopore matrix. The influence of the microscopic roughness is shown in Fig. 4(a) for clean-cut kerogen samples. The results show that scattering on a higher density kerogen, results in a lower degree of tangential momentum accommodation, due to the lower
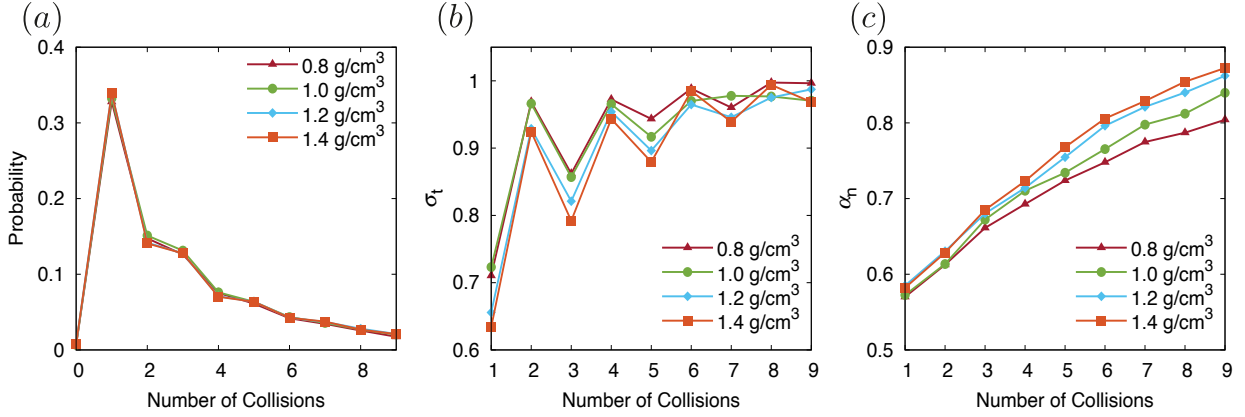
11

Figure 6: Distribution of the number of collisions during the scattering of methane molecules inside the near-surface layer on EFK kerogen samples, without considering the mesoscopic roughness for pressure $P_0 = 0.75$ MPa (a) Probability density distribution of number of collisions. (b) The TMAC versus number of collisions. (c) The accommodation of the normal kinetic energy versus number of collisions.

porosity (i.e., microscopic roughness). In Fig. 4(a), a lower TMAC is also observed for molecules with higher incident velocities, which is consistent with the literature [14, 26]. However, as seen in Fig. 4(b), there is a negligible effect of a kerogen's microscopic roughness on the degree of accommodation for the kinetic energy normal to the surface. This may occur because the exchange of energy between methane molecules and kerogen atoms represented by α_n^p mostly depends on the intermolecular force field and the fluid-wall mass ratio, which remain relatively constant across kerogen samples. A singular-like behaviour can be observed when the impinging velocity is close to the most probably speed. However, this behaviour is a numerical artefact that is likely due to the numerical inaccuracies arising in this condition as both numerator and denominator in Eqn. (7) approach to zero [25, 26, 50].

In this work, the mesoscopic roughness is controlled in a simple, albeit unphysical way, by carving the kerogen sample using a two-dimensional corrugated surface:

$$\Delta z = \frac{A}{2} \left[\sin\left(\frac{2\pi x}{p}\right) + \sin\left(\frac{2\pi y}{p}\right) \right]. \tag{8}$$

This simplified approach provides insights into the sensitivity of roughness on the accommodation coefficients, and the expected transition from a partial to a fully-accommodating wall. According to Eqn. (8), and shown also in Fig. 5(a), the topographic roughness is determined by two parameters, i.e., the amplitude A and the period p of the corrugated surface. The pore width, H thus is defined as the distance between the centrelines (i.e., $z = 0$ on bottom and $z = H$ on top) of the sinusoidal curves, or between the centre of the outermost atoms for limiting cases with no mesoscopic roughness (i.e. when the amplitude $A = 0$). Figs. 5(b-c) show that with increasing amplitude and smaller period of mesoscopic roughness, the TMAC rapidly increases and approaches unity. More importantly, since the porosity of the considered samples ($\phi = 14\%$ - 45%) has a small effect on TMAC, then the limiting cases with no mesoscopic roughness, which have a TMAC > 0.8, leads us to conclude that a high degree of accommodation for tangential momentum will be a common feature for any type of kerogen surface. Note that this conclusion becomes even more

12

accurate for lower reservoir temperatures (i.e., $T_w < 423$ K), which also can be found in shale applications, as the accommodation coefficients (e.g., TMACs) generally become larger at lower T_w [14]. Compared to the tangential momentum, the amplitude and period of the mesoscopic roughness have less influence on the accommodation of normal kinetic energy, as shown in Figs. 5(d-e).

Generally, momentum and energy is exchanged between gas molecules and the surface during collisions. Therefore, the number of collisions suffered by gas molecules with the surface during their residence time offers further insights on the dependence of accommodation coefficients on the molecules' impinging patterns (i.e., single or multiple collisions). Fig. 6(a) shows that a methane molecule may collide with the surface atoms more than once. Moreover, for the scattering process, about a third of methane molecules undergo a single collision, whereas most of them collide with the surface multiple times, thus losing memory of their incoming velocity. This high probability of multiple collisions is also found to be mostly independent on the porosity of the kerogen surface. Figs. 6(b-c) show that, under a fixed number of collisions, a higher TMAC was obtained for the kerogen surface with a higher porosity (microscopic roughness), while α_n decreases with porosity. Moreover, the TMACs approach unity rapidly with an increasing number of collisions, whereas the increase of accommodation of normal kinetic energy α_n is much slower. This difference in accommodation verifies the idea that momentum is being lost or gained much faster than energy in physical interactions [25]. Finally, Fig. 6(c) shows that, in the first few collisions that cover most cases of scattering situations, α_n on kerogen surfaces with various microscopic roughness are close to each other, which explains why the partial α_n^p (Fig. 4(b)) and global α_n (Figs. 5(d-e)) are relatively constant across kerogen samples.

4.3. Deviations of velocity distributions from conventional kernels

Scattering kernels can be assessed by comparing the predicted scattering pattern of a molecular beam against MD simulation results. Here, the accommodation coefficients that enter in the scattering kernels (i.e., the Maxwell, CL and Yamamoto models) are given the values obtained by our MD simulations (Fig. 4). Similar to the evaluation of partial accommodation coefficients, we first take incident molecules with a velocity between $V_i^* - \Delta V^*$ and $V_i^* + \Delta V^*$, where the small increment $\Delta V^* = 0.1$, and investigate the velocity distribution after reflection for these molecules only. Here, we choose normalised velocities 0.1, 0.5, 0.9, 1.4 and 1.9. Fig. 7(a) shows the reflected velocity distributions for all the incident velocities considered. The results show that the tangential velocity distributions at small incident velocities are nearly symmetric and their centrelines are close to $V_{t,r}^* = 0$. Figs. 7(b-d) show that all the scattering kernels provide relatively good fits to those distributions resulting from small incident velocities, which are expected due to the high TMACs. Small discrepancies are only observed for the small $V_{t,r}^*$, indicating that the magnitude of the tangential velocity is partially retained during the scattering process. By contrast, Figs. 7(e-f) shows that no existing scattering kernel could reproduce a distribution for molecules with high incident velocity. These disagreements at high incident speeds were also found for scattering of Xe atoms on GaSe [54], and N_2 on Pt surface [26]. In addition, a Maxwell or Epstein model [27] contains a component of specular reflection, which would appear as a spike-like pattern in the velocity distributions of Fig. 7. This pattern is not discernible in our MD results, which indicates that
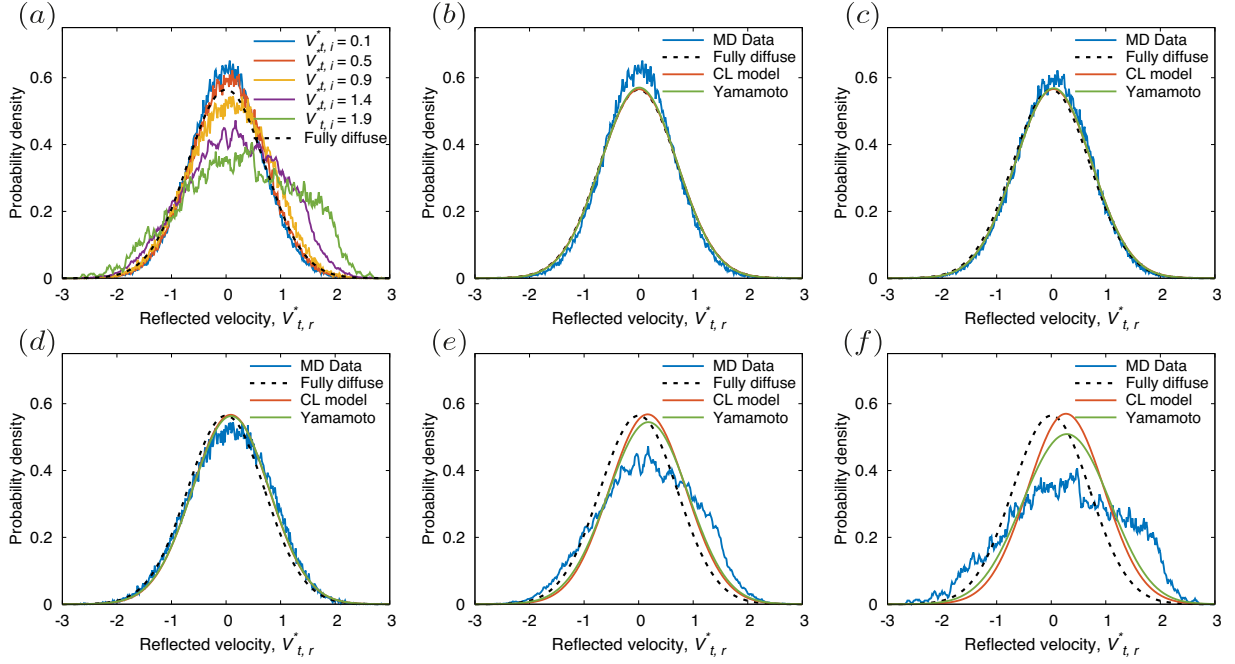
13

Figure 7: Comparison of reflected tangential velocity distributions predicted by MD and existing scattering kernels with accommodation coefficients obtained by MD. (a) MD results due to various incident velocity magnitudes; (b) $V_{t,i}^* = 0.1$, $\sigma_t^P = 0.9230$; (c) $V_{t,i}^* = 0.5$, $\sigma_t^P = 0.9194$; (d) $V_{t,i}^* = 0.9$, $\sigma_t^P = 0.9024$; (e) $V_{t,i}^* = 1.4$, $\sigma_t^P = 0.882$; and (f) $V_{t,i}^* = 1.9$, $\sigma_t^P = 0.8581$. Note that the Maxwell model with a calibrated TMAC is not presented, as the spike-like pattern of specular reflection is clearly not observed in our MD results. All the MD results are obtained from the scattering on kerogen structure EFK 0.8 g/cm^3 with roughness amplitude $A = 4$ Å, period $p = 25$ Å.

any scattering kernel that in an ad hoc manner, proposes to incorporate a component of specular reflection will not be an exact predictor of the scattering behaviour on kerogen surfaces.

Fig. 8 shows the normal velocity distributions of reflected molecules. The incident velocity magnitudes of the normal component $|V_{n,i}^*|$ are kept the same as the tangential velocity values. Fig. 8(a) shows the distributions for all the selected incident velocities. As $V_{n,i}^*$ increases, the peak of the distribution shifts to higher reflected velocities $V_{n,r}^*$ and the curve flattens. As shown in Fig. 8(b), no scattering kernel is able to capture the reflection pattern of molecules with low incident velocity. This may be because the existence of the attractive force field, which decelerates the molecules in the direction normal to the surface and partially suppresses the reflection of molecules at small $V_{n,r}^*$. While the effects of this strong interaction cannot be fully predicted by a scattering kernel in the limit of small impinging velocities, the CL model seems to provide satisfactory comparisons from moderate to high incident velocities, as shown in Figs. 8(c-f).

To understand the interplay between normal and tangential velocity components that significantly influences the gas transport in porous media [55–57], we next investigate the scattering angular distributions of the reflected molecules, as shown in Fig. 9. The representative incident angle θ_i are taken to be $15°, 30°, 45°, 60°$ and $75°$ with respect to the
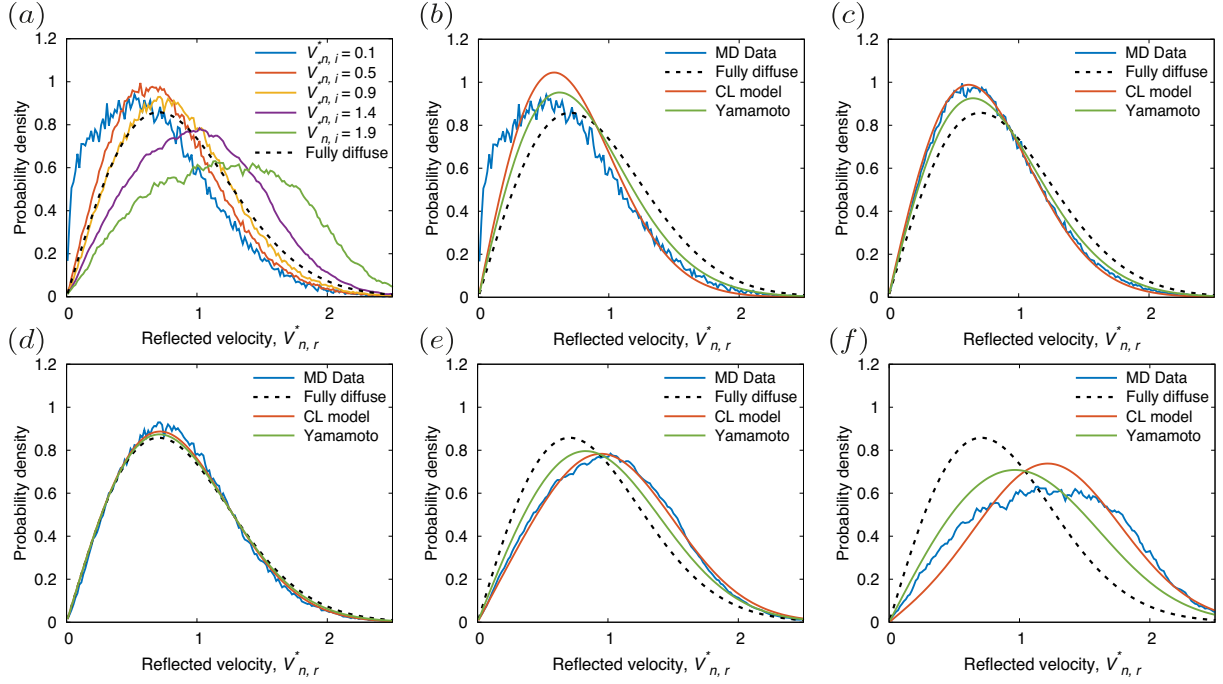
14

Figure 8: Comparison of reflected normal velocity fluxes predicted by MD and existing scattering kernels with accommodation coefficients obtained by MD. (a) MD data due to various incident velocity magnitudes; (b) $V_{n,i}^* = 0.1$, $\alpha_n = 0.68$; (c) $V_{n,i}^* = 0.5$, $\alpha_n = 0.68$; (d) $V_{n,i}^* = 0.9$, $\alpha_n = 0.68$; (e) $V_{n,i}^* = 1.4$, $\alpha_n = 0.68$; and (f) $V_{n,i}^* = 1.9$, $\alpha_n = 0.68$. MD results are obtained on kerogen structure EFK 0.8 g/cm^3 ($A = 4$ Å, $p = 25$ Å).

surface normal. The scattering angle distributions can be calculated by the following equation

$$\theta_r = \arctan\left(\frac{|v_n|}{|v_t|}\right). \tag{9}$$

The range of the scattering angle thus becomes $[0°, 90°]$. Unlike most beam experiments [54, 58, 59], at which the scattering angle strongly depends on the incident angle of the gas molecule, Fig. 9(a) shows that distribution patterns due to different incident angles coincide with each other. The reason for this may be twofold: (a) the incident velocity in our simulations is relatively low, in contrast with beam experiments, where the impinging speed is normally high and leads to an increase in lobe peak height, and (b) the reflection pattern is considerably affected by the adsorption, micro- and mesoscopic roughness of the porous kerogen matrix, whereas most beam experiments consider a clean, smooth non-porous surface. Moreover, these angular scattering distributions based on our MD results are found to be very close to the fully-diffuse scattering kernel, even though the accommodation coefficients (i.e., σ_t, α_n) are smaller than unity. Nevertheless, these angular distribution measurements again confirm that the high degree of accommodation is one of the main characteristics during the scattering process of methane with kerogen. Under such a high degree of accommodation, all scattering kernels that satisfy the basic relations (i.e., positiveness, normalisation and the detailed balance – see Appendix A) should get similar results and approach the fully-diffuse scattering kernel.
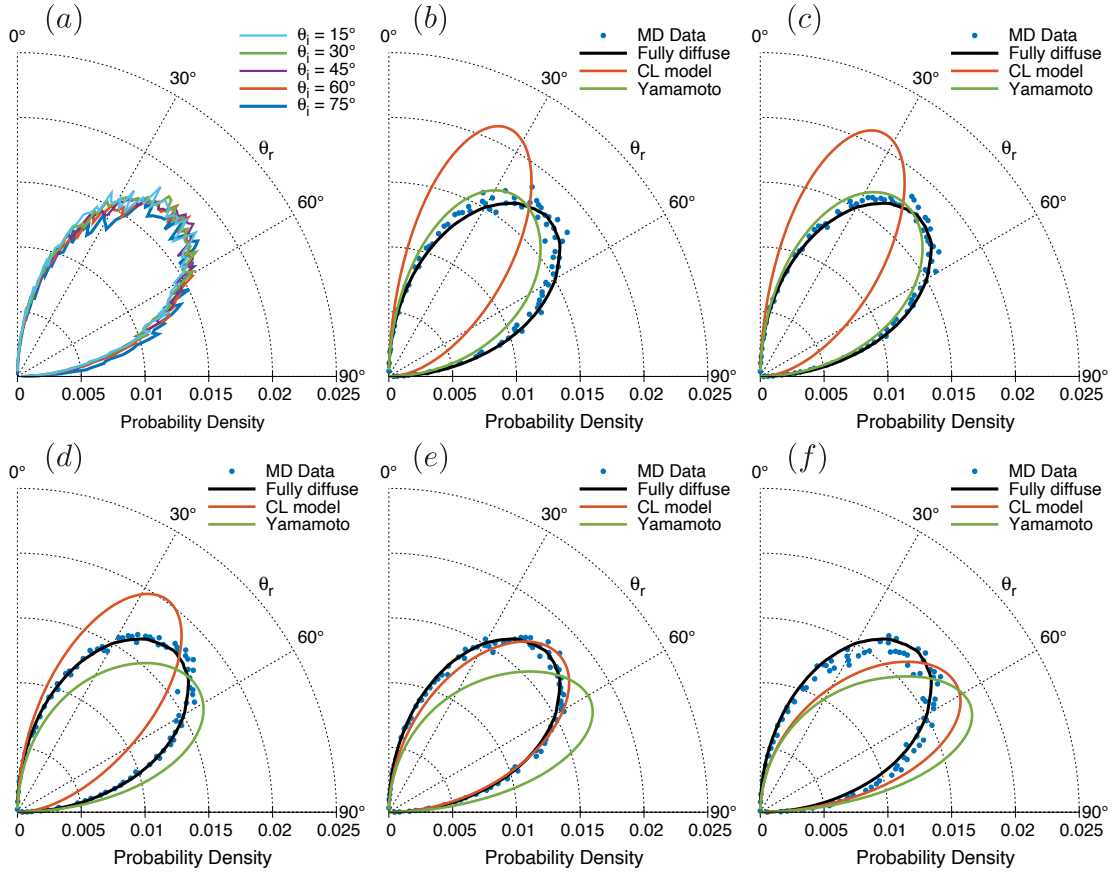
15

Figure 9: Comparison of reflected angular distributions predicted by (a) MD and (b-f) existing scattering kernels $\theta_i = 15°, 30°, 45°, 60°, 75°$. MD results are obtained on kerogen structure EFK 0.8 g/cm^3 ($A = 4$ Å, $p = 25$ Å).

4.4. Impact of Maxwell scattering kernel on flow transport

Although our results indicate that no single classical scattering kernel could capture the detailed scattering of methane with kerogen, a high degree of accommodation was observed during the gas-surface interactions in all our simulations. Additionally, it is more important to capture the reflected angular distribution, which reflects the interplay between different velocity components and can be modelled by the quasi-fully-diffuse scattering kernel for rough surfaces, than independently capturing the distribution for each velocity component [55–57]. It may also be more appropriate to adopt a fully-diffuse model, which is simpler to implement for gas transport models. Here, we investigate the effect of the scattering physics on gas transport, when there is a force-driven Poiseuille flow inside the set-up of Fig. 1(a). Two cases are initially considered with an external force $F_0 = 2.0 \times 10^{-14}$ N, 8.0×10^{-14} N applied on each atom in the $x-$direction, leading to an average bulk velocity $U_x^* = 0.25, 0.60$, respectively. In Fig. 10(a), it is seen that the overall incident tangential velocity distribution follows a shifted diffuse scattering profile accommodated to a temperature higher than the kerogen surface, as a result of the external force. The overall reflected velocity distribution, however, lies in between the incident velocity distribution and the prediction from the fully-diffuse scattering kernel
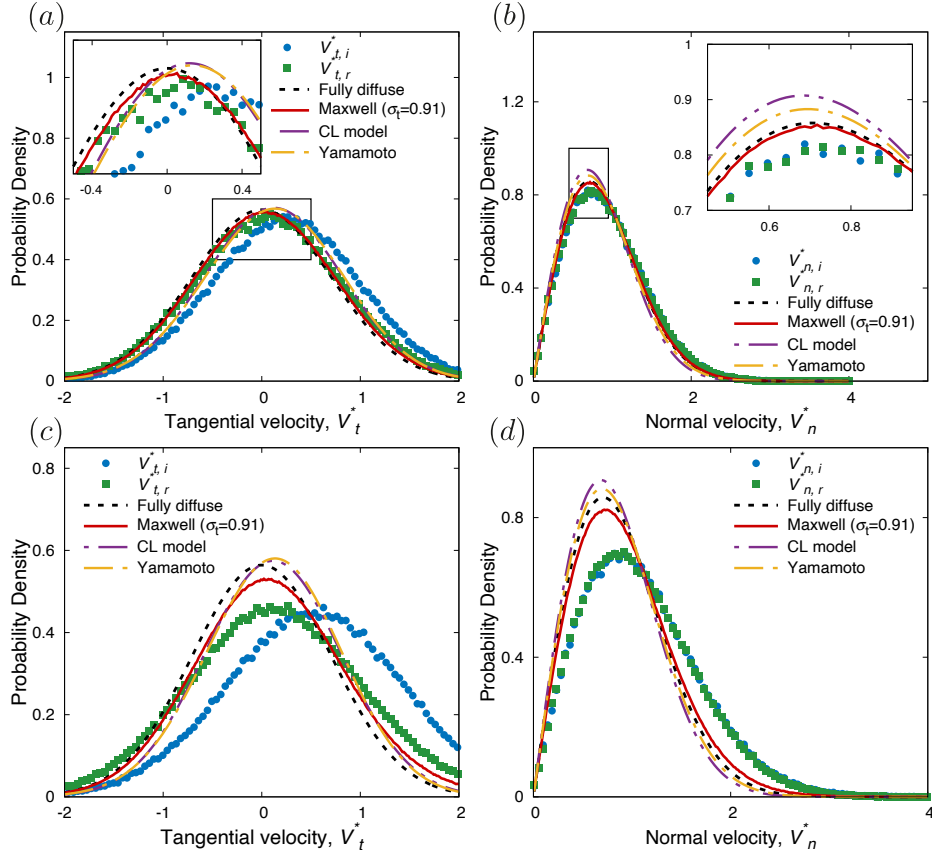
16

Figure 10: Overall velocity distributions from MD in Poiseuille flow, with bulk velocity and accommodation coefficients for (a-b) the low speed case ($U_x^* = 0.25$, $\sigma_t = 0.91$, $\alpha_n = 0.68$), and (c-d) the high speed case ($U_x^* = 0.6$, $\sigma_t = 0.91$, $\alpha_n = 0.68$). MD results are obtained on kerogen structure EFK 0.8 g/cm^3 ($A = 4$ Å, $p = 25$ Å). Note that the global accommodation coefficients (σ_t, α_n) in this transport study are also interpreted as the equilibrium ones based on the kerogen structure, for which the corresponding values are shown in Fig. 5.

(i.e., Maxwell model with TMAC = 1). To find the best fit of the reflected velocity distribution, the profiles predicted by the Maxwell, CL and Yamamoto models are also drawn. It is observed that the simplest Maxwell model, with TMAC calibrated from our MD, turns out to reproduce a better overall fit than the other two kernels. This observation indicates that the Maxwell model may be sufficient in practical applications for gas transport near a kerogen surface, even though, as discussed, its detailed scattering pattern is not realistic due to the incorporation of a small specular reflection component. For the direction normal to the surface, Fig. 10(b) shows that incident and reflected velocity distributions are very close to each other. This overlap may be because the gas molecules are difficult to accommodate their normal kinetic energy with the surface in the first few collisions (see Section 4.2), especially under a bulk velocity. Moreover, although the CL model could provide satisfactory predictions for selected incident normal velocities without considering the gas transport (Fig. 8), the Maxwell model seems to give the closest agreement of the overall reflected velocity distribution for transport cases. It is noteworthy that the Maxwell model also gives good agreements for both tangential and normal components of the overall velocity distributions for nitrogen gas scattering on platinum walls
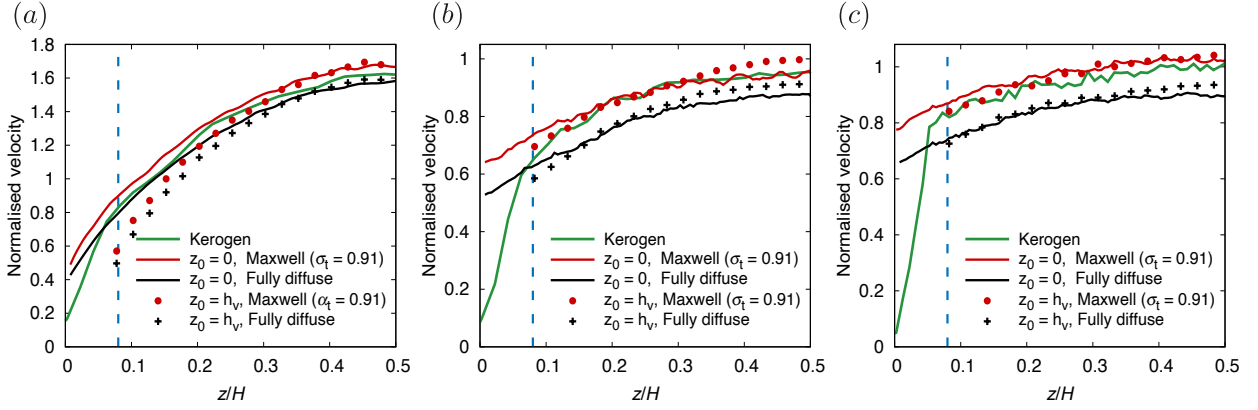
17

Figure 11: Profiles of normalised velocity for gas flow with Kn = (a) 0.12, (b) 0.63, and (c) 6.25. The vertical dashed line within each plot represents the virtual plane ($z_0 = h_v$). The solid lines represents the velocity profiles for a pore height of H = 20 nm (i.e., boundary located at $z_0 = 0$), while the scatter points represent the velocity profiles for a pore height of $H - 2h_v$ = 17 nm (where the boundary is located at $z_0 = h_v$). To include the effect of pore size, here we apply a reference velocity V_0, which is assumed to be proportional to the normalised pressure gradient $\zeta = F_0 H / (k_B T_0)$ and the most probable speed V_m, i.e., $V_0 = \zeta V_m$. All the profiles are obtained from the flow on the kerogen structure EFK 0.8 g/cm^3 (A = 4 Å, p = 25 Å).

[41]. As a comparison to the distributions of low speed flows, Figs. 10(c-d) show large disagreements between the reflected velocity distributions and profiles of existing scattering kernels for a high speed flow. This disagreement is expected from previous selected velocity distribution measurements. However, these high speed flows are rarely encountered in shale gas extraction and can safely be ignored, which we verify in the next part of this section.

Another perspective for investigating the effects of scattering physics on transport properties is by analysing velocity profiles across the pore, which are shown in Fig. 11 for a representative set of Knudsen numbers, i.e., Kn = [0.12, 0.63, 6.25]. These cases are selected to cover a significant range of gas rarefaction and specifically highlight the comparison between the MD flow transport simulations of methane through kerogen mesopores (as in Fig. 1(a)), and the equivalent MD simulations where the porous kerogen surfaces are now replaced by a scattering model instead. For these benchmark cases, the boundary condition is defined as a non-porous mathematical planar wall, and the Maxwell scattering model with TMAC calibrated from our scattering analysis. We choose MD to compare both types of simulations (instead of using DVM or DSBGK kinetic solvers, which assume the hard sphere or variable hard sphere collision dynamics) in order to keep the same gas-gas interactions (those of an LJ model), while only changing the wall boundary condition. Furthermore, we do not pick other distributions (CL, Yamamoto), because our previous analysis indicates that the simplest Maxwell model provides the best prediction of the overall reflected velocity distribution that is sufficient for the transport study. An important remark needs to be made here. Mathematical boundaries that are used to model the gas-surface interaction should, in principle, be placed at the virtual plane, i.e., the location at which the scattering information was measured. However, this choice is not ideal, because shale rock surfaces (measured from experiments) will need to be translated by a distance h_v, which — depending on

18

the pore size — may influence the permeability apart from making it complex to implement numerically. Having different pore heights also makes the comparison of transport in our study more challenging. Here, we present velocity profile results for both pore heights (H and $H - 2h_v$, which correspond to the location of the boundary at $z_0 = 0$ and $z_0 = h_v$, respectively) to test the scattering kernel, and discuss the implications of this shortly.

330   For flows with a moderately confined pore and a relatively high gas pressure (P_0 = 3.92 MPa), which correspond to Kn = 0.12 (Fig. 11(a)), we can see that all three types of surfaces produce a parabolic-like profile. In the bulk, both the Maxwell (TMAC = 0.91) and fully-diffuse model give good agreements with the kerogen results for $z_0 = 0$, while the models implemented at $z_0 = h_v$ do not agree well. When the rarefaction level increases to Kn = 0.63 and 6.25, as shown in Fig. 11(b) and Fig. 11(c) respectively, the differences between boundary implementations ($z_0 = 0$, $z_0 = h_v$)
335   becomes small in the bulk region of the flow. While the agreement between the kerogen surface and Maxwell model remains good, the deviation of the fully-diffuse model from the kerogen surface becomes noticeable at large Kn.

In Fig 11, the velocity profiles near the kerogen surface drop very rapidly within h_v to a finite but small slip value near the wall. This may be caused by the high adsorption force field, and it is expected the slip value will approach zero when a larger surface roughness (e.g., > 2 nm) is involved [60]. From these figures, it is clear that none of the
340   scattering models can predict the transport in this near-surface layer, which means the location of the boundary will always be marred by modelling inaccuracies within h_v. On one hand, if the boundary is located at $z_0 = h_v$ to correctly satisfy the condition of imposing scattering where it is measured, we will miss out on mass transport due to geometrical differences for these moderately confined cases; e.g., for Kn = 0.63, we have a 5-8% drop in mass transport. On the other hand, if we place the boundary at $z_0 = 0$, we can recover some but never the exact local mass flow rate inside
345   the near-surface layer because the local velocity and density profiles obtained by the scattering boundary model do not account for adsorption effects. At larger pore sizes, the difference about whether choosing $z_0 = h_v$ or $z_0 = 0$ does not matter, as $h_v/H \approx 0$ and the adsorption effects and flow rates in the near-surface layer become negligible on the overall transport. For the remaining part of the paper, we will choose the location of $z_0 = 0$ as it shows better overall agreement in the velocity profiles, has less effect on the mass flow rate for moderately-sized pores and is the most
350   practical to implement in future kinetic solvers. Furthermore, we pick the Maxwell model with TMAC calibrated from our MD, as the TMAC for the simulated kerogen surface with very small roughness is still less than unity.

Finally, we show the normalised mass flow rate Q^* in Fig. 12, as a direct indicator of the impact of the scattering kernel on flow transport, across a wide range of Knudsen numbers. Comparisons are made between the MD simulations of the kerogen sample (EFK 0.8 g/cm^3, A = 4 Å, p = 25 Å), the calibrated Maxwell model of this sample (TMAC = 0.91)
355   and the fully-diffuse model (TMAC = 1) using MD simulations with simplified boundaries and the linearised Boltzmann equations (LBE) [61]. Because TMAC is not expected to change significantly with Kn, particularly for rough surfaces, it is fixed for all Knudsen numbers. In Fig. 12, the predictions given by the simplified MD simulations (LJ potentials + fully-diffuse) agree well with the results predicted by LBE (hard-sphere molecules + fully-diffuse) before the flow is highly-rarefied, indicating the Boltzmann and its model equations are indeed applicable for mesospores with negligible
360   confinement effect (e.g., $H \sim 20$ nm). Moreover, a general trend can be found that Q^*, given by the kerogen surface,
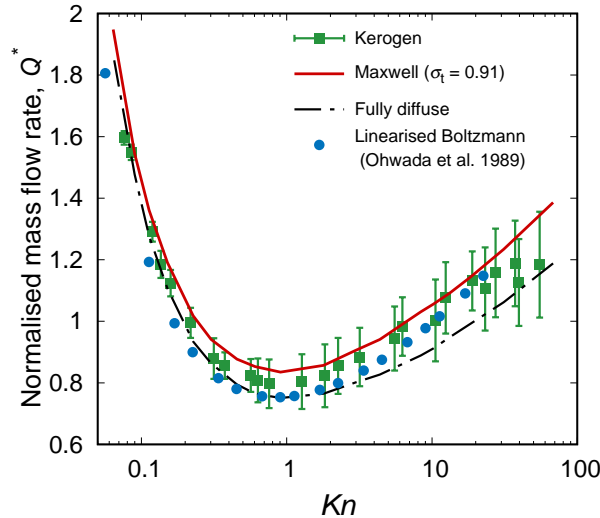
19

Figure 12: Dependence of the normalised mass flow rate on gas rarefaction Kn for kerogen structure EFK 0.8 g/cm^3 with a roughness amplitude $A = 4$ Å and period $p = 25$ Å. The mass flow rate Q was measured in the linear response regime (i.e., low-speed, isothermal flows) as the spatial integration of local density, area, and velocity, using discretised bins along the $z-$direction. The normalised mass flow rate therefore is defined as $Q^* = Q/Q_0$, where $Q_0 = mn_0V_0HL_y$ is the reference factor, and L_y is the depth of the simulation domain.

lies between the predictions given by the Maxwell and the fully-diffuse models, with a minimum value observed at $Kn \approx 1$. When Kn is small (i.e., within the slip and early transition flow regimes), the mass flow rate due to different surfaces are close to each other. This phenomenon is also confirmed in the work of Wu *et al.,*[35], where similar results are observed for various scattering kernels at TMAC = 0.92 based on the LBE with the LJ potential of helium. Therefore, one may deduce that when the flow system is less-rarefied, an arbitrary scattering kernel (satisfying the basic properties) will provide adequate accuracy for the prediction of mass flow rate within shale, while the Maxwell model certainly is the simplest to implement numerically. As Kn increases to the free molecular regime, it is seen that the Maxwell model (TMAC = 0.91) agrees better with the mass flow rate from the kerogen surface, than the same model (implemented by MD and LBE) with TMAC = 1. It is worth noting that as the mesoscopic roughness increases from the assumed 0.4 nm to ~ 2 nm, the TMAC will approach unity, at which the results of both kerogen surface and Maxwell model should converge to the prediction of the fully diffuse model. However, the flow rate predicted by both Maxwell and fully diffuse model have noticeable discrepancy from the kerogen surface results when the flow is highly rarefied ($Kn > 10$), which suggests that the dominant Knudsen diffusion mechanism [9, 55, 57] is now revealing the inaccuracies in the scattering dynamics of these models.

5. Conclusions and remarks

We have investigated the scattering dynamics and accommodation of methane molecules on realistic kerogen surfaces, which contained porosities and mesoscopic roughness to enable the description of gas-surface interactions. Existing scattering kernels have been assessed by comparing the reflected velocity fluxes and evaluating their impact

on the gas transport properties, using Molecular Dynamics (MD) simulations. We summarise our conclusions as follows:

- For re-emitted methane gas molecules, the residence time and displacement due to adsorption/desorption are on average unaffected by porosity; thus, gas-surface interactions on kerogen can be considered instantaneous in time and local in space, as assumed by conventional scattering kernels.

- The most widely used scattering kernel are found unable to describe the detailed scattering behaviours on kerogen surfaces, especially the reflected velocity fluxes of high speed flows, and to a lesser extent, some of the lower speeds due to the kerogen's force field.

- The Maxwell model comes closest to the observed scattered angular beam pattern (under a TMAC = 1) and the overall reflected velocity distribution (under a TMAC calibrated by our MD), which are both more important when considering the transport study, than correctly capturing the individual velocity component fluxes.

- The Maxwell model satisfactorily predicts the velocity profiles and overall mass flow rate for the transport cases confined between kerogen surfaces for a wide range of Knudsen numbers Kn, despite the observed deviation at large Kn, which, however, is a condition that is seldom met in shale reservoirs.

This paper, therefore, confirmed the applicability of the diffuse-specular Maxwell model to deal with gas transport in organic shale media, even though the underlying scattering dynamics was found to be more sophisticated. Moreover, given the fact that the TMAC was observed to approach unity at atomic-scale roughness of $\Delta z \sim 2$ nm, as also reported on the study of other surfaces [53, 57], the fully-diffuse Maxwell scattering kernel may also be appropriate for modelling gas transport near kerogen or other mineral surfaces. This work also settles the question as to what value of TMAC should be used in gas transport near organic kerogen surfaces, and further investigations will be required when calibration studies with experiments reveal TMACs much lower than 1.0. For this to be true, there has to be a high concentration of very smooth non-organic surfaces, which we believe is unlikely in shale rock.

Appendix A. Basic properties of the scattering kernel

In rarefied gas dynamic solvers, the kinetic boundary condition is generally expressed via a scattering kernel $R(\boldsymbol{v}' \rightarrow \boldsymbol{v})$ as [25]

$$v_n f(\boldsymbol{v}) = \int_{v_n' < 0} |v_n'| R(\boldsymbol{v}' \rightarrow \boldsymbol{v}) f(\boldsymbol{v}') d\boldsymbol{v}', \quad v_n > 0, \tag{A.1}$$

where v_n' and v_n are the incident and reflected velocity components normal to the surface. The scattering kernel $R(\boldsymbol{v}' \rightarrow \boldsymbol{v})$ satisfies the following basic properties:

(a) Positiveness:

$$R(\boldsymbol{v}' \rightarrow \boldsymbol{v}) \geq 0, \tag{A.2}$$

(b) Normalisation:

$$\int_{v_n > 0} R(\boldsymbol{v}' \rightarrow \boldsymbol{v}) d\boldsymbol{v} = 1, \tag{A.3}$$

which means the surface is impermeable and gas molecules are not permanently adsorbed.

(c) Reciprocity:

$$|v_n'| f_0(T_w, \boldsymbol{v}') R(\boldsymbol{v}' \rightarrow \boldsymbol{v}) = |v_n| f_0(T_w, \boldsymbol{v}) R(-\boldsymbol{v} \rightarrow -\boldsymbol{v}'), \tag{A.4}$$

where

$$f_0(T_w, \boldsymbol{v}) = \exp\left(-\frac{m|\boldsymbol{v}|^2}{2k_B T_w}\right) \tag{A.5}$$

is the Maxwellian velocity distribution function (VDF) with zero velocity in the reference system at rest with respect to the wall, m is the molecular mass of the gas particles, k_B is the Boltzmann constant and T_w is the temperature of the wall.

This property is also called the "reciprocity law" or the "detailed balance", which states that if the gas is in equilibrium with the wall, the number of molecules scattered from a velocity range $[\boldsymbol{v}', \boldsymbol{v}' + d\boldsymbol{v}']$ to a velocity range $[\boldsymbol{v}, \boldsymbol{v} + d\boldsymbol{v}]$ (per unit area and unit time) is equal to the number of molecules scattered from any velocity within $[-\boldsymbol{v}, -\boldsymbol{v} - d\boldsymbol{v}]$ to a velocity within $[-\boldsymbol{v}', -\boldsymbol{v}' - d\boldsymbol{v}']$ [62, 63].

References

[1] K. Falk, B. Coasne, R. Pellenq, F.-J. Ulm, L. Bocquet, Subcontinuum mass transport of condensed hydrocarbons in nanoporous media, Nature Communications 6 (1) (2015) 1–7.

[2] C. Guo, J. Xu, K. Wu, M. Wei, S. Liu, Study on gas flow through nano pores of shale gas reservoirs, Fuel 143 (2015) 107–117.

[3] S. Wang, F. Javadpour, Q. Feng, Molecular dynamics simulations of oil transport through inorganic nanopores in shale, Fuel 171 (2016) 74–86.

[4] S. Wang, F. Javadpour, Q. Feng, Fast mass transport of oil and supercritical carbon dioxide through organic nanopores in shale, Fuel 181 (2016) 741–758.

[5] Y. Liu, Z. Jin, H. A. Li, Comparison of peng-robinson equation of state with capillary pressure model with engineering density-functional theory in describing the phase behavior of confined hydrocarbons, SPE Journal 23 (05) (2018) 1784–1797.

[6] B. Shan, R. Wang, Z. Guo, P. Wang, Contribution quantification of nanoscale gas transport in shale based on strongly inhomogeneous kinetic model, Energy 228 (2021) 120545.

[7] Y. Liu, J. Hou, C. Wang, Absolute adsorption of CH4 on shale with the simplified local-density theory, SPE Journal 25 (01) (2020) 212–225.

[8] X. Huang, L. Gu, S. Li, Y. Du, Y. Liu, Absolute adsorption of light hydrocarbons on organic-rich shale: An efficient determination method, Fuel 308 (2022) 121998.

[9] C. Corral-Casas, L. Gibelli, M. K. Borg, J. Li, S. F. Al-Afnan, Y. Zhang, Self-diffusivity of dense confined fluids, Physics of Fluids 33 (8) (2021) 082009.

[10] Z. Liehui, S. Baochao, Z. Yulong, G. Zhaoli, Review of micro seepage mechanisms in shale gas reservoirs, International Journal of Heat and Mass Transfer 139 (2019) 144–179.

[11] Y. Yang, K. Wang, L. Zhang, H. Sun, K. Zhang, J. Ma, Pore-scale simulation of shale oil flow based on pore network model, Fuel 251 (2019) 683–692.

[12] A. S. Ziarani, R. Aguilera, Knudsen's permeability correction for tight porous media, Transport in porous media 91 (1) (2012) 239–260.

[13] C. Freeman, G. Moridis, T. Blasingame, A numerical study of microscale flow behavior in tight gas and shale gas reservoir systems, Transport in Porous Media 90 (1) (2011) 253–268.

[14] B.-Y. Cao, J. Sun, M. Chen, Z.-Y. Guo, Molecular momentum transport at fluid-solid interfaces in mems/nems: a review, International Journal of Molecular Sciences 10 (11) (2009) 4638–4706.

[15] Z. Jin, A. Firoozabadi, Flow of methane in shale nanopores at low and high pressure by molecular dynamics simulations, The Journal of Chemical Physics 143 (10) (2015) 104315.

[16] L. Wu, H. Liu, J. M. Reese, Y. Zhang, Non-equilibrium dynamics of dense gas under tight confinement, Journal of Fluid Mechanics 794 (2016) 252–266.

[17] Q. Sheng, L. Gibelli, J. Li, M. K. Borg, Y. Zhang, Dense gas flow simulations in ultra-tight confinement, Physics of Fluids 32 (9) (2020) 092003.

[18] P. Wang, M. T. Ho, L. Wu, Z. Guo, Y. Zhang, A comparative study of discrete velocity methods for low-speed rarefied gas flows, Computers & Fluids 161 (2018) 33–46.

[19] M. T. Ho, L. Zhu, L. Wu, P. Wang, Z. Guo, J. Ma, Y. Zhang, Pore-scale simulations of rarefied gas flows in ultra-tight porous media, Fuel 249 (2019) 341–351.

[20] J. Li, Efficient prediction of gas permeability by hybrid DSBGK-LBM simulations, Fuel 250 (2019) 154–159.

[21] S. Livadiotti, N. H. Crisp, P. C. Roberts, S. D. Worrall, V. T. Oiko, S. Edmondson, S. J. Haigh, C. Huyton, K. L. Smith, L. A. Sinpetru, et al., A review of gas-surface interaction models for orbital aerodynamics applications, Progress in Aerospace Sciences 119 (2020) 100675.

[22] J. C. Maxwell, Vii. on stresses in rarified gases arising from inequalities of temperature, Philosophical Transactions of the Royal Society of London (170) (1879) 231–256.

[23] C. Cercignani, M. Lampis, Kinetic models for gas-surface interactions, Transport Theory and Statistical Physics 1 (2) (1971) 101–114.

[24] J. Li, M. T. Ho, M. K. Borg, C. Cai, Z.-H. Li, Y. Zhang, Pore-scale gas flow simulations by the DSBGK and DVM methods, Computers & Fluids (2021) 105017.

[25] C. Cercignani, Gas-surface interaction and the H-theorem, in: The Boltzmann equation and its applications, Springer, 1988, pp. 104–157.

[26] K. Yamamoto, H. Takeuchi, T. Hyakutake, Scattering properties and scattering kernel based on the molecular dynamics analysis of gas-wall interaction, Physics of Fluids 19 (8) (2007) 087102.

[27] M. Epstein, A model of the wall boundary condition in kinetic theory, AIAA Journal 5 (10) (1967) 1797–1800.

[28] T. Klinc, I. Kuščer, Slip coefficients for general gas-surface interaction, The Physics of Fluids 15 (6) (1972) 1018–1022.

[29] M. Gallis, J. Torczynski, D. Rader, An approach for simulating the transport of spherical particles in a rarefied gas flow via the direct simulation monte carlo method, Physics of Fluids 13 (11) (2001) 3482–3492.

[30] S. K. Dadzie, J. G. Méolans, Anisotropic scattering kernel: Generalized and modified maxwell boundary conditions, Journal of Mathematical Physics 45 (5) (2004) 1804–1819.

[31] H. Struchtrup, Maxwell boundary condition and velocity dependent accommodation coefficient, Physics of Fluids 25 (11) (2013) 112001.

[32] R. Lord, Some extensions to the cercignani–lampis gas–surface scattering kernel, Physics of Fluids A: Fluid Dynamics 3 (4) (1991) 706–710.

[33] R. Lord, Some further extensions of the cercignani–lampis gas–surface interaction model, Physics of Fluids 7 (5) (1995) 1159–1161.

[34] A. Yakunchikov, V. Kovalev, S. Utyuzhnikov, Analysis of gas-surface scattering models based on computational molecular dynamics, Chemical Physics Letters 554 (2012) 225–230.

[35] L. Wu, H. Struchtrup, Assessment and development of the gas kinetic boundary condition for the boltzmann equation, Journal of Fluid Mechanics 823 (2017) 511–537.

[36] J. Wang, L. Chen, Q. Kang, S. S. Rahman, The lattice boltzmann method for isothermal micro-gaseous flow and its application in shale gas flow: A review, International Journal of Heat and Mass Transfer 95 (2016) 94–108.

[37] R. N. Moghaddam, M. Jamiolahmady, Study of slip flow in unconventional shale rocks using lattice boltzmann method: Effects of boundary conditions and TMAC, Transport in Porous Media 120 (1) (2017) 115–139.

[38] H. Darabi, A. Ettehad, F. Javadpour, K. Sepehrnoori, Gas flow in ultra-tight shale strata, Journal of Fluid Mechanics 710 (2012) 641–658.

[39] J. Ma, J. P. Sanchez, K. Wu, G. D. Couples, Z. Jiang, A pore network model for simulating non-ideal gas flow in micro-and nano-porous materials, Fuel 116 (2014) 498–508.

[40] L. Wu, M. T. Ho, L. Germanou, X.-J. Gu, C. Liu, K. Xu, Y. Zhang, On the apparent permeability of porous media in rarefied gas flows, Journal of Fluid Mechanics 822 (2017) 398–417.

[41] K. Yamamoto, H. Takeuchi, T. Hyakutake, Characteristics of reflected gas molecules at a solid surface, Physics of Fluids 18 (4) (2006) 046103.

[42] T. Liang, Q. Li, W. Ye, A physical-based gas–surface interaction model for rarefied gas flow simulation, Journal of Computational Physics 352 (2018) 105–122.

[43] C. Bousige, C. M. Ghimbeu, C. Vix-Guterl, A. E. Pomerantz, A. Suleimenova, G. Vaughan, G. Garbarino, M. Feygenson, C. Wildgruber, F.-J. Ulm, et al., Realistic molecular model of kerogen's nanostructure, Nature Materials 15 (5) (2016) 576–582.

[44] S. Plimpton, Fast parallel algorithms for short-range molecular dynamics, Journal of Computational Physics 117 (1) (1995) 1–19.

[45] A. Obliger, F.-J. Ulm, R. Pellenq, Impact of nanoporosity on hydrocarbon transport in shales' organic matter, Nano Letters 18 (2) (2018) 832–837.

[46] J. Sun, Z.-X. Li, Effect of gas adsorption on momentum accommodation coefficients in microgas flows using molecular dynamic simulations, Molecular Physics 106 (19) (2008) 2325–2332.

[47] R. Wang, J. Li, L. Gibelli, Z. Guo, M. K. Borg, Sub-nanometre pore adsorption of methane in kerogen, Chemical Engineering Journal 426 (2021) 130984.

[48] Y. Liu, H. A. Li, Y. Tian, Z. Jin, H. Deng, Determination of the absolute adsorption/desorption isotherms of CH4 and n-C4H10 on shale from a nano-scale perspective, Fuel 218 (2018) 67–77.

[49] H.-J. Butt, K. Graf, M. Kappl, Adsorption, in: Physics and chemistry of interfaces, John Wiley & Sons, 2003, pp. 177–205.

[50] P. Spijker, A. J. Markvoort, S. V. Nedea, P. A. Hilbers, Computation of accommodation coefficients and the use of velocity correlation profiles in molecular dynamics simulations, Physical Review E 81 (1) (2010) 011203.

[51] L. B. Thomas, R. Lord, Comparative measurements of tangential momentum and thermal accommodations on polished and on roughened steel spheres, Rarefied Gas Dynamics 8 (1974) 405–412.

[52] A. Agrawal, S. Prabhu, Survey on measurement of tangential momentum accommodation coefficient, Journal of Vacuum Science & Technology A: Vacuum, Surfaces, and Films 26 (4) (2008) 634–645.

[53] J. Sun, Z.-X. Li, Three-dimensional molecular dynamic study on accommodation coefficients in rough nanochannels, Heat Transfer Engineering 32 (7-8) (2011) 658–666.

[54] D. Bruno, M. Cacciatore, S. Longo, M. Rutigliano, Gas-surface scattering models for particle fluid dynamics: a comparison between analytical approximate models and molecular dynamics calculations, Chemical Physics Letters 320 (3-4) (2000) 245–254.

[55] G. Arya, H.-C. Chang, E. J. Maginn, Knudsen diffusivity of a hard sphere in a rough slit pore, Physical Review Letters 91 (2) (2003) 026102.

[56] F. Celestini, F. Mortessagne, Cosine law at the atomic scale: toward realistic simulations of knudsen diffusion, Physical Review E 77 (2)

(2008) 021202.

[57] T. Liang, Q. Li, Accurate modeling of knudsen diffusion in nanopores using a physical-based boundary model, Journal of Applied Physics 126 (8) (2019) 084304.

[58] H. Saltsburg, J. N. Smith Jr, Molecular-beam scattering from the (111) plane of silver, The Journal of Chemical Physics 45 (6) (1966) 2175–2183.

[59] H. Yu, Y. Zhang, F. Yang, H. Li, Molecular dynamics study on scattering characteristics of nitrogen molecules from platinum surface by molecular beam method, AIP Advances 10 (9) (2020) 095028.

[60] H. Yu, H. Xu, J. Fan, F. Wang, H. Wu, Roughness factor-dependent transport characteristic of shale gas through amorphous kerogen nanopores, The Journal of Physical Chemistry C 124 (23) (2020) 12752–12765.

[61] T. Ohwada, Y. Sone, K. Aoki, Numerical analysis of the poiseuille and thermal transpiration flows between two parallel plates on the basis of the boltzmann equation for hard-sphere molecules, Physics of Fluids A: Fluid Dynamics 1 (12) (1989) 2042–2049.

[62] I. Kuščher, Reciprocity in scattering of gas molecules by surfaces, Surface Science 25 (2) (1971) 225–237.

[63] F. Sharipov, Onsager-casimir reciprocity relations for open gaseous systems at arbitrary rarefaction: I. general theory for single gas, Physica A: Statistical Mechanics and its Applications 203 (3-4) (1994) 437–456.